J. Plasma Phys. (2023), *vol*. 89, 955890601

Published by Cambridge University Press

doi:10.1017/S0022377823001010

Using rational surfaces to improve pellet fuelling in stellarators

N. Panadero [1],†, K. J. McCarthy [1], B. Pégourié[2], R. Carrasco [1], I. García-Cortés [1], R. García[1], J. Hernández-Sánchez[1], F. Köchl[3], J. Martínez-Fernández[1], R. Sakamoto [4] and the TJ-II team

[1]Laboratorio Nacional de Fusión, CIEMAT, Madrid, Spain

[2]CEA, IRFM, F-13108 Saint-Paul-lez-Durance, France

[3]ITER Organization, Route de Vinon-sur-Verdon, CS 90 046, 13067 Saint-Paul-lez-Durance Cedex, France

[4]National Institute for Fusion Science, Toki, Japan

(Received 31 October 2022; revised 24 August 2023; accepted 25 August 2023)

Pellet injection is currently the primary candidate for achieving efficient plasma fuelling, one of the key issues for steady-state operation in large fusion devices. In this paper, pellet injection experiments are performed for several magnetic configurations of the TJ-II stellarator. The aim of this study is to increase the understanding of the role played by rational surfaces in plasmoid drift and deposition profiles in stellarators. The analysis of experimentally observed plasmoid drifts is supported by simulations of such cases made with the HPI2 code. Plasmoid drift is found to be significantly reduced, as in tokamaks, in the vicinity of rational surfaces. This is attributed to the fact that plasmoid external charge reconnection lengths are shorter near rational surfaces, resulting in a more effective damping of the plasmoid drift. Although the effect of plasmoid external currents on the drift is expected to be negligible in stellarators, compared with those caused by plasmoid internal currents, the effect observed in TJ-II is clearly measurable. In addition, simulations show that enhanced drift reductions near rational surfaces lead to significantly different deposition profiles for the magnetic configurations included in this study. This implies that it should be possible to select the magnetic configurations to obtain more efficient pellet fuelling.

Key words: fusion plasma, plasma confinement

1. Introduction

An efficient fuelling capability is mandatory for stationary operation in large magnetic-confinement fusion devices to achieve the conditions required for fusion. Fuelling is expected to be especially important for helical-type machines since, according

† Email address for correspondence: nerea.panadero@ciemat.es

to neoclassical theory, core particle depletion is expected when employing microwave central heating (Maaßberg, Beidler & Simmet 1999). However, the situation may not be so critical since a later study indicates that turbulent transport contributes to avoid such depletion (Thienpondt *et al.* 2023). Cryogenic pellet injection is currently the best candidate for achieving efficient fuelling, as it leads to deeper fuelling penetration and higher fuelling efficiencies than can be achieved with other existing methods (Mikkelsen *et al.* 1995). In the case of pellet injection, the final positions where particles are deposited, as well as overall fuelling efficiency, depend strongly on the $\nabla \boldsymbol{B}$-induced drift of the ionised pellet material. Therefore, understanding all the mechanisms affecting this drift, such as reductions caused by external plasmoid currents, is critical for the development of optimised fuelling schemes in future fusion devices.

When a pellet enters magnetically confined plasma, it is ablated by interaction with background plasma particles. This ablated material expands around the pellet, protecting it from further interactions with the ambient plasma, thereby reducing the ablation rate and increasing the pellet lifetime (Pégourié 2007). During this time, this neutral cloud is ionised and, as the ionisation degree increases, the ionised fraction of the cloud or plasmoid starts expanding along the magnetic field lines until plasma and plasmoid pressure reach equilibrium (Milora *et al.* 1995; Pégourié 2007). At the same time, during the homogenisation process, this plasmoid drifts down the magnetic field gradient, which was firstly observed by Müller *et al.* (1999). The resultant $\nabla \boldsymbol{B}$-drift arises from a modification of the potential distribution inside a plasmoid (Rozhansky *et al.* 2004; Parks & Baylor 2005; Pégourié *et al.* 2007). For arbitrary magnetic configurations, the main term of cloud drift acceleration is given by (Köchl *et al.* 2012; Matsuyama *et al.* 2012*a*)

$$\frac{\mathrm{d}\boldsymbol{v}_{\mathrm{drift}}}{\mathrm{d}t} = \frac{\frac{\mathrm{d}\boldsymbol{E}}{\mathrm{d}t} \times \boldsymbol{B}_\infty}{B_\infty^2} = -\frac{2(p_0 - p_\infty)\nabla_\perp \boldsymbol{B}_\infty}{n_0 m_i B_\infty}. \tag{1.1}$$

However, several mechanisms can either enhance (Parks & Baylor 2005) or reduce (Rozhansky *et al.* 2004; Senichenkov *et al.* 2005; Pégourié *et al.* 2007) the drift acceleration by modifying this potential distribution. In particular, when the electric potential perturbation of the plasmoid invades the entire magnetic surface and the plasmoid becomes large enough to cover a significant poloidal and toroidal angular sector, two processes arise that provide effective drift damping. On the one hand, internal plasmoid currents arise to balance the variation of charge accumulation on the plasmoid surface due to the rotation of magnetic field lines around the plasmoid centre. In more detail, when the plasmoid length exceeds a critical size, $L_c \cong \pi q R$, the relative direction of the $\nabla \boldsymbol{B}$ associated current are inverted at the two ends of the plasmoid, and the circuit is closed by a parallel current inside the plasmoid, reducing the drift velocity (Rozhansky *et al.* 2004; Senichenkov *et al.* 2005). This damping effect, referred to here as the internal circuit closure (ICC) effect, is important for plasmoids with very long parallel lengths or for short plasmoid–internal charge reconnection lengths. On the other hand, an external current arises when, due to the finite plasmoid cross-section, regions of opposite polarisation start to become interconnected along the magnetic field lines (Pégourié *et al.* 2007). In another way, when two positively charged regions are connected along the same flux tube, the circuit is closed by a parallel resistive current along the same flux tube, which dampens the drift. This effect will be referred to here as the external circuit closure (ECC) effect. This ECC effect takes place when regions of opposite polarisation become connected with each other, on a time scale longer than the time of first connection, $\tau_{\mathrm{con}} \approx \pi R m / C_A$, which corresponds to a plasmoid reconnection length of $L_{\mathrm{con}} \approx 2\pi R m$ (here, C_A is the Alfvén speed and m is the poloidal mode number). This effect was

https://doi.org/10.1017/S0022377823001010 Published online by Cambridge University Press

evident in the works of Commaux *et al.* (2010) and Sakamoto *et al.* (2013) through its correlation with the radial distribution of rational magnetic flux surfaces. Indeed, the relation between the iota profile and deposition profiles is explained by the dependence of the drift displacement on the magnetic-field lines connection length, which in turn depends on the local iota value. In another way, in the vicinity of rational values, where the connection length is significantly reduced, the ECC mechanism is more efficient at reducing the drift acceleration. This implies that ablated material tends to be further accumulated near these rational surfaces. The term in the drift equation (in addition to (1.1) and expressions for the other additional terms; Panadero *et al.* 2023) related to the ECC effect, are given, in a simplify way, by (for more detail expression see Panadero *et al.* 2023)

$$\frac{\mathrm{d}\boldsymbol{v}_{\mathrm{drift}}^{\mathrm{ECC}}}{\mathrm{d}t} = -\boldsymbol{v}_{\mathrm{drift}}\left(\frac{\sigma_{\infty}B^2\pi R_0^2}{2n_0m_0Z_0Z_{\infty}}\right). \tag{1.2}$$

Here, σ_∞ is the plasma parallel conductivity and B is the background magnetic field, R_0 is the plasmoid radius, n_0 is the plasmoid density and m_0 is the ion mass. In addition, Z_0 is the plasmoid parallel length and Z_∞ the length of the flux tube connecting the two ends of the plasmoid. Here, Z_∞ is bounded by $2\pi^2 Ra/R_0$, where R and a are the major and minor radii of the plasma. However, close to the integer rational surfaces, it decreases down to $2\pi qR$, where q is the safety factor, which explains the aforementioned major role of the iota profile in stopping the drift (Geulin & Pegourie 2022). The drift-damping produced by external currents is the dominant effect in tokamaks, whereas internal currents are dominant in helical configurations due to their shorter plasmoid–internal charge reconnection lengths (Matsuyama *et al.* 2012*a*). However, a previous study in TJ-II revealed an interaction between outward-drifting plasmoids and low-order rational surfaces that can be attributed to the ECC effect (McCarthy *et al.* 2021). Therefore, plasmoid deceleration by low-order rational surfaces cannot always be considered a minor effect in stellarators.

In this work, the damping of plasmoid drift due to external currents is studied in TJ-II, both experimentally and theoretically. For this, cryogenic pellets are injected into different TJ-II magnetic configurations and drifting plasmoids are followed with a high-speed camera. In parallel, the HPI2 code (Pégourié *et al.* 2005; Pégourié *et al.* 2007; Köchl *et al.* 2012) is used to simulate pellet injections into the same configurations of this device. The HPI2 code can simulate both pellet ablation and plasmoid homogenisation in a consistent way, considering also the specific geometrical data, the plasma density and temperature profiles as well as the magnetic configuration of a particular device (Pégourié *et al.* 2005; Pégourié *et al.* 2007; Köchl *et al.* 2012). First, the ablation rate is calculated using an enhanced version of the Neutral Gas and Plasma Shielding (NGPS) model (Pégourié *et al.* 2005; Köchl *et al.* 2012), for each position considered along its injection trajectory. For this, the plasma particle distribution is considered by separating it into discrete groups of mono-energetic beams and following each beam through all the layers surrounding the pellet. Plasmoid dimensions and internal parameters, later used as input for the homogenisation calculations, are also obtained. Afterwards, the evolution of the plasmoid, once it is detached from the pellet, i.e. when it evolves independently from the pellet, is followed using a two-cell four-fluid Lagrangian model (Lengyel 1978; Pégourié *et al.* 2007; Köchl *et al.* 2012), by considering mass and energy conservation laws. In addition, plasmoid drift is calculated taking into consideration the fact that the drift and the plasmoid expansion are coupled through the dependence of the drift on the difference between plasmoid and plasma pressures. Therefore, the motion of the plasmoid barycentre is calculated self-consistently with the evolution of the plasmoid and the plasma (Pégourié

https://doi.org/10.1017/S0022377823001010 Published online by Cambridge University Press

et al. 2007; Köchl *et al.* 2012). To give a complete picture of the plasmoid evolution, the HPI2 model includes, in addition to the main drift term ((1.1)), the curvature enhancement provoked by plasmoid parallel expansion, the damping effect of Alfvén wave emission, and the ICC and ECC effects (see (1.2)) (Panadero *et al.* 2023). Furthermore, the effect of the various additional mechanisms that dampen plasmoid drift can be evaluated by omitting the corresponding term in the drift equation. For instance, when assessing the impact of the ECC effect, the terms in (1.2) can be neglected in the simulation, i.e. these terms are set to zero. In addition to this, for non-axisymmetric devices, the toroidal variation of the $\nabla \boldsymbol{B}$-drift is included in the calculation of the plasmoid drift, although in a simplified way. In particular, an effective drift is assumed for all plasmoid particles, regardless of their toroidal position, by toroidally averaging all geometric- and magnetic-related quantities (Panadero *et al.* 2023). This stellarator version of HPI2, which has already been validated for TJ-II ECRH scenarios (Panadero *et al.* 2018), is used in this work. Note that the validation for NBI scenarios is pending, although the ablation model has been tested in, for instance, LHD, with promising results (Matsuyama *et al.* 2012*b*). The aim of this study is to evaluate the effect of rational surfaces on fuelling efficiency and on particle deposition in stellarators, and to assess whether it is possible to modify the magnetic configuration so as to optimise pellet fuelling.

In the paper, the experimental set-up is described in § 2. In §§ 3 and 4, experimental results into selected TJ-II magnetic configurations and the results of the pellet injection simulations for these same configurations are presented, respectively. Finally, conclusions are presented and discussed in § 5.

2. Experimental set-up

In this work, pellet injection experiments are carried out in the stellarator TJ-II to clarify the influence of rational surfaces on plasmoid drift and pellet fuelling efficiency. The TJ-II is a powerful tool for undertaking such studies as a broad variety of rotational transforms can be obtained. In addition, representative experimental results are compared with simulations performed with the HPI2 code. In this section, the TJ-II stellarator is described, together with its pellet injection system and associated diagnostics relevant for this study.

2.1. *The TJ-II stellarator*

The TJ-II is a four-period, low magnetic shear ($\Delta\iota \leq 6\,\%$) stellarator located at CIEMAT, Madrid, Spain (Hidalgo *et al.* 2022). Its major radius, R_0, is 1.5 m, and its average minor radius, a_0, is $\leq$0.22 m. A set of poloidal, toroidal and vertical coils creates its fully three-dimensional magnetic field with a bean-shaped cross-section, central magnetic field, $B(0) \leq 1.1$ T, and total plasma volume of approximately 1.1 m^3. These coils allow a wide range of vacuum magnetic configurations to be obtained and permit exploration of a broad variety of rotational transforms, $0.9 \leq \iota(0)/2\pi \leq 2.2$. Plasmas, usually of hydrogen and with a typical duration of $\leq$300 ms, are created and maintained using electron cyclotron resonance heating (ECRH) and/or neutral beam injection (NBI). The two gyrotrons that form the ECRH system ($P_{\mathrm{ECRH}} \leq 500$ kW, $t_{\mathrm{discharge}} \leq 300$ ms) operate at 53.2 GHz, the second harmonic of the electron cyclotron resonance frequency for $B = 1.1$ T. The central electron densities, $n_e(0)$, and temperatures, $T_e(0)$, that can be achieved are $\leq 1.7 \times 10^{19}$ m^{-3} and $\leq$2 keV, respectively. The NBI system consists of two tangential injectors, one operated in counter configuration, the other in co-counter configuration ($E_{\mathrm{NBI}} \leq 32$ keV, $P_{\mathrm{NBI}} \leq 0.7$ MW throughput). Central electron densities and temperatures of $n_e(0) \leq 5 \times 10^{19}$ m^{-3} and $T_e(0) \leq 400$ eV, when a lithium coating is applied to the vacuum vessel wall (Tabarés *et al.* 2010), can be achieved. The central ion temperature,

https://doi.org/10.1017/S0022377823001010 Published online by Cambridge University Press

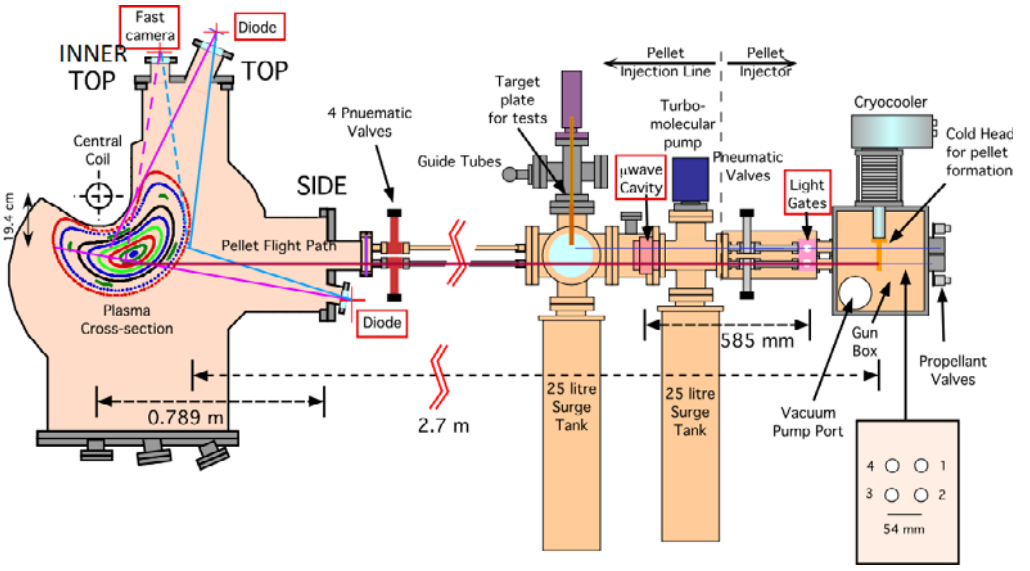

FIGURE 1. Cross-sectional sketch of the TJ-II vacuum chamber (left) with closed magnetic surfaces and the pellet injector. The relative locations of pellet Lines 1–4 are indicated with respect to the rear of the PI at the bottom right. Reproduced courtesy of IAEA. Figure from McCarthy *et al.* (2017). © 2017 Centro de Investigaciones Energéticas Medioambientales y Tecnológicas.

$T_i(0)$, achieved with both heating schemes, is $\leq\sim$120 eV. Under these conditions, relatively good density control and plasma reproducibility are achieved (Tabarés *et al.* 2008).

2.2. *The TJ-II pellet injection system and associated diagnostics.*

The TJ-II pellet injector (PI) is a four-barrel pipe gun device with a cryogenic refrigerator for *in situ* pellet formation (10 K), fast propellant valves for pellet acceleration (velocities between 800 m s^{-1} and 1200 m s^{-1} can be achieved) and straight delivery lines. It is a flexible system, since it allows injecting, from the outer side of the device, pellets of four different sizes (nominal pellet particle content ranges from 4×10^{18} to 4.1×10^{19} H atoms) along four different injection lines (labelled Lines 1 to 4, see figure 1 (Combs *et al.* 2013; McCarthy *et al.* 2017). In this work, only injection Line 1 is used (see figure 2*a*).

The PI is equipped with an in-line diagnostic system which is formed by a light gate and a microwave cavity to estimate pellet velocity and mass (Combs *et al.* 2013). In addition, two amplified silicon photodiodes, fitted with interference filters centred at 660 nm (with full-width at half-maximum transmission width of 10 nm), follow, from above (TOP) and behind (SIDE) the pellet flight path, the Balmer H_α ($\lambda = 656.28$ nm) emitted by the pellet cloud (McCarthy *et al.* 2015*a*; Panadero *et al.* 2018). In addition, an ultra-fast CMOS camera, model FASTCAM APX-RS by Photron Incorporation, San Diego, CA, records fast-frame images of injected pellets. For this, it is equipped with a coherent fibre double bundle and machine-vision type camera lenses (e.g. 12.5 mm lens, model HF12.5SA-1 by Fujinon Tokyo, Japan) (Panadero *et al.* 2018, 2021). Lenses can be located above, behind and/or tangential to the flight path, thus allowing pellet and plasmoid to be recorded simultaneously from two different viewports. This camera is able to record at frame rates of between 50 frames s^{-1} at full frame (1024 × 1024 pixels) and 250 kilo-frames s^{-1} (kfps) at reduced frame (128 × 16 pixels), where each pixel corresponds to ∼0.5 mm to ∼1 mm

https://doi.org/10.1017/S0022377823001010 Published online by Cambridge University Press

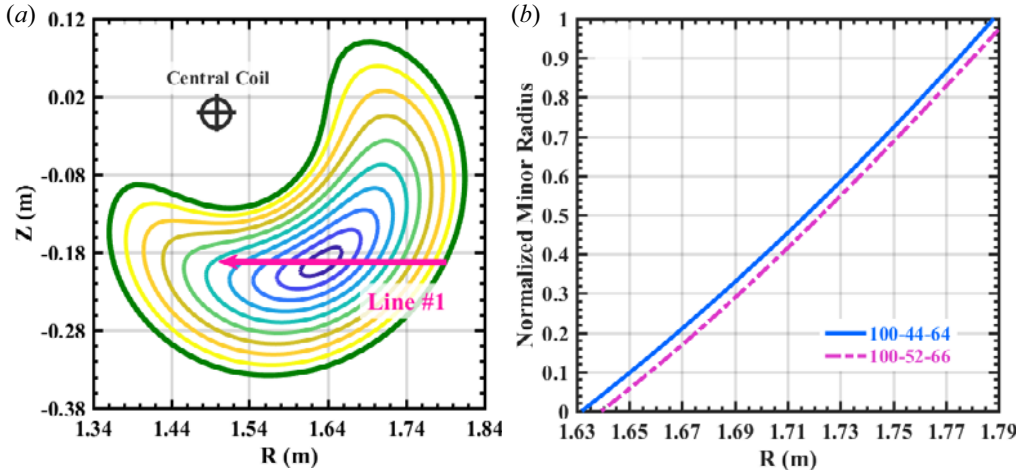

FIGURE 2. (*a*) Closed magnetic flux surfaces for the 100_44_64 magnetic configuration at the toroidal position where pellets are injected. The configuration label 'xxx_yy_zz' represents currents in hundreds of Amperes in the circular, helical and vertical field coils of TJ-II. Expected pellet flight path for injection Line 1 is shown. (*b*) Relation between the R co-ordinate and normalised minor radius for the pellet injection Line 1 (note that the Z coordinate remains constant, i.e. $Z = -0.194$ m for the complete pellet trajectory) for 100_44_64 (continuous blue line) and 100_52_66 (dash-dotted magenta line) configurations.

along the pellet flight path, depending on the viewport. In addition, it is possible to control the exposure time of the electronic shutter independently, from $1/v$ s, where v is the frame rate (in frame s^{-1}), to 1 μs. The field of view of the fast camera and photodiodes is shown in figure 1. Finally, the quality of the spatial calibration of the camera set-up has been reported by Panadero *et al.* (2018).

3. Experimental results

The injection of hydrogen pellets was performed into ECRH and NBI hydrogen plasmas created using different TJ-II magnetic configurations to observe and measure variations in plasmoid drift when a pellet crosses a rational surface. From the broad range of magnetic configurations available in TJ-II, results for the 100_44_64 (standard) and 100_52_66 configurations are presented here. Iota profiles of these configurations, together with some of the main low-order rational surfaces, are shown in figure 3. As noted above, in-line light-gate and microwave cavity signals are used to establish pellet timing and mass, while ablation profiles are determined from the recorded Balmer H_α emission (McCarthy *et al.* 2015*a*). For that, it is considered that a pellet is not radially accelerated inside the plasma, i.e. it is assumed that the pellet speed is constant, which is a reasonable assumption as shown by Panadero *et al.* (2018).

Plasmoid drift can be observed in TJ-II with the fast camera when, for the current experimental set-up, very high temporal resolution and low exposure time, ≤ 1 μs, are used. This means that drift can only be estimated at the beginning of the homogenisation process, i.e. during the ≤ 1 μs exposure time (it should be noted that for an exposure time of 1 μs and a mean pellet speed of the order of 1 km s^{-1}, pellet movement across the camera detector is less than one pixel). At this time, $t = 1$ μs, the typical plasmoid length is in the range of 0.1 m $\leq Z_0 \leq$ 0.2 m, and hence regions of opposite polarisation have already connected to each other, as seen in figure 4. i.e. the ECC effect has already

https://doi.org/10.1017/S0022377823001010 Published online by Cambridge University Press

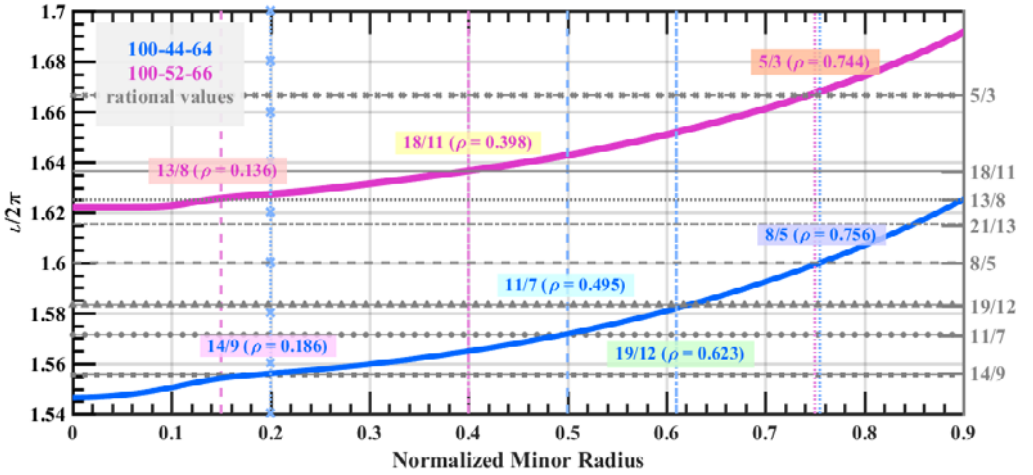

FIGURE 3. Iota profiles corresponding to the three TJ-II magnetic configurations used during pellet injection experiments. The standard TJ-II configuration (100_44_64) is plotted in blue and the 100_52_66 in magenta. Principal low order rational surfaces are also indicated (horizontal grey lines and vertical blue, green and magenta lines).

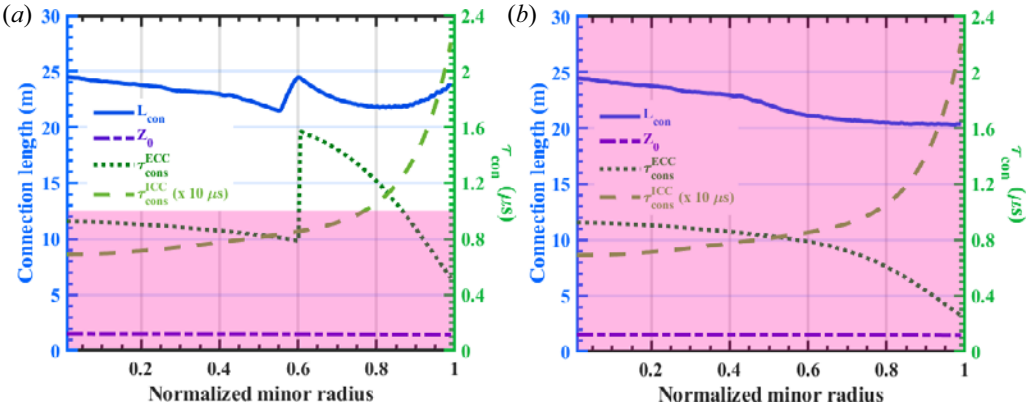

FIGURE 4. Theoretical connection length (solid blue) for the ECC effect and connection times (dotted dark green) for a plasmoid having (*a*) 0.1 m of parallel length and (*b*) 0.2 m of parallel length, as calculated by HPI2. For comparison, the minimum plasmoid length, Z_0, for which the ICC effect appears ($Z_0 \geq \pi R_0 q/2$, where R_0 and q are device major radius and local safety factor, respectively) and the connection time for such an effect are included as dash-dotted purple and dashed lime green lines, respectively. The shaded areas highlight the regions for which the ECC connection time is ≤ 1 μs.

started to take place by this time (see § 1). In this figure, it can also be observed that, for such plasmoid lengths, the connection time for the ICC effect is approximately an order of magnitude longer than for the ECC effect. Although a detached plasmoid can be detected sometimes, a drifting plasmoid is usually observed as an asymmetry of the cloud (see figure 5*a*). From this asymmetry, the initial drift displacement can be estimated. For this purpose, it is assumed that the main contribution to the light intensity of the cloud is due to the ablation of the pellet, and that there is a secondary contribution attributed to the partially ionised drifting plasmoid. Taking this into account, the light profile recorded by

https://doi.org/10.1017/S0022377823001010 Published online by Cambridge University Press

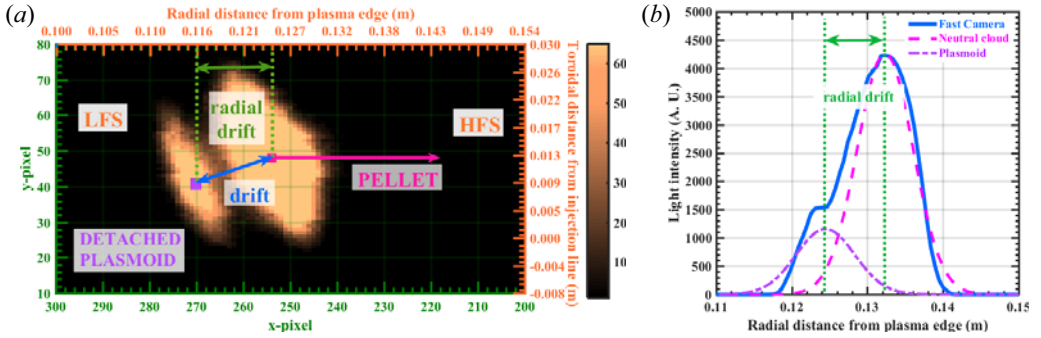

FIGURE 5. (*a*) Snap-shot image (frame rate = 50 kfps, exposure time 1 μs) taken from the INNER TOP viewport versus distance into the plasma (the injection direction – towards the high-field side (HFS) – is indicated by the magenta arrow) for a pellet with 7.76×10^{18} H atoms injected into discharge 53344 at 933 m s^{-1} along Line 1 during a balanced NBI heating phase. Two emission regions are seen, one from the neutral cloud (right) and the other from a plasmoid (left). Plasmoid drift towards the low-field side (LFS) of the plasma can be appreciated (indicated by the blue double arrow, while the radial component of the drift is represented by a green double arrow). (*b*) Integrated light emission profile from fast-camera images (solid blue line), which corresponds to the light emitted by the neutral cloud surrounding the ablating pellet plus the emission from a drifting plasmoid for discharge 53344. The ablation (dashed magenta line) and plasmoid (dash-dotted purple line) contributions are obtained by fitting two Gaussian profiles to the blue profile. The distance between the centres of the two Gaussians (highlighted by vertical dotted green lines) is equivalent to the radial drift displacement, indicated by the green double arrow.

the camera is fitted by two Gaussians, the difference between the two centres being the drift, as explained by Panadero *et al.* (2018) (see also figure 5*b*). Here, only images taken from the INNER TOP view are considered, i.e. only the radial component of the drift is estimated from the cloud asymmetry in the radial (horizontal in the image) direction. It should also be noted that no toroidal drift is expected, as the main component of the magnetic field is directed along the toroidal direction. In addition, sometimes a small toroidal (vertical in the image) deviation may appear in an image, however, this can be attributed to an artefact from the poloidal drift of the plasmoid.

Representative cases for pellet injection into the TJ-II configurations 100_44_64 (standard configuration) and 100_52_66 will be shown here for balanced NBI plasmas. Pellet injections into ECRH plasmas are not included in this paper as such plasmas have relatively high electron temperatures in TJ-II, i.e. up to 1.5 keV, this resulting in increased ablation rates and hence moderately high initial plasmoid pressures and shallow penetration depths (Panadero *et al.* 2018). This translates into rapid plasmoid expansion and large initial drift accelerations. Therefore, it is not the most suitable scenario to study plasmoid drift in detail, as it requires high frame rates and low exposure times that are very challenging with the current set-up available. In contrast, when pellets are injected into balanced NBI-heated plasmas, plasmoid expansion and drift are significantly reduced due to the lower plasma electron temperature, which leads to lower ablation rates and initial plasmoid pressures (as compared with ECRH cases). Therefore, it is possible to increase the camera frame rate and to obtain better temporal resolutions, i.e. a larger number of data points. Consequently, this is the scenario chosen to study plasmoid drift. Starting with the standard TJ-II configuration, the radial plasmoid drift displacement, averaged for a series of reproducible discharges (from 53344 to 53349), is shown in figure 6, together with the

https://doi.org/10.1017/S0022377823001010 Published online by Cambridge University Press

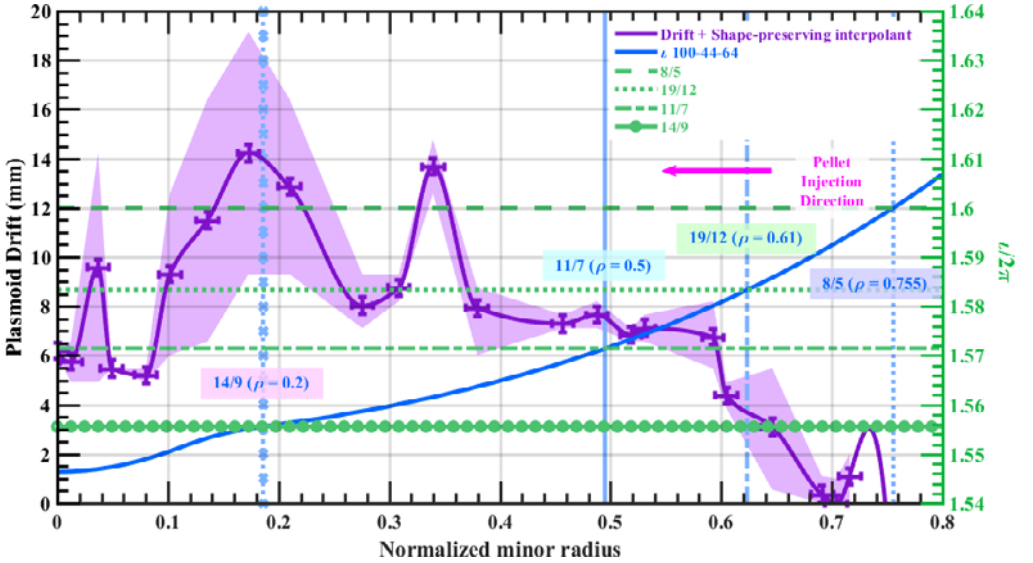

FIGURE 6. Radial plasmoid drift displacement as a function of pellet radial position, estimated from fast-camera images for the TJ-II 100_44_64 configuration (standard configuration) for a series of reproducible discharges (53344 to 53349). Calculated drift values are plotted in purple, with the corresponding error bars, while a connection between points is made with a continuous purple line (shaded region represents the dispersion in the data). The iota profile for this configuration is plotted in solid blue. The strongest low-order rational values in this iota interval are highlighted using horizontal dashed, dotted, dash-dotted and solid with circles green lines, and vertical dotted, dash-dotted, dash and dotted with crosses blue lines. The pellet injection direction is indicated by a magenta arrow.

standard configuration iota profile and the strongest low-order rational surfaces crossed in this configuration. Here, the estimated radial drift shown indicates the radial drift for a plasmoid detached at the position given by the horizontal axis, i.e. a plasmoid drift value of 14 mm at $\rho = 0.18$ indicates that the plasmoid detached at $\rho = 0.18$ undergoes a radial drift of 14 mm after 1 μs. These pellets where injected along Line 1 with a mean hydrogen content of $\sim 8.8 \times 10^{18}$ atoms and a mean speed of ~ 920 m s^{-1}. These injections were recorded by the fast camera with a frame rate between 50 and 150 kfps, and an exposure time of 1 μs for the whole series. In figure 6, it can be observed that the drift displacement tends to generally increase with pellet penetration depth up to $\rho = \sim 0.5$, as the drift increases with increasing electron temperature. However, between $\rho = \sim 0.4$ and $\rho = \sim 0.6$, the drift displacement remains mostly constant. This can be attributed to a combination of the effect of rational surfaces, which limit the drift, and faster ionisation of the plasmoid with higher electron temperatures, i.e. plasmoids are visible in the fast camera for a shorter period of time due to the more rapid ionisation (although, in reality, plasmoid drift increases with plasma electron temperature). In addition, some local minima are observed at certain radial positions. These drift reductions could be accounted for by the effect of the rational surfaces in the vicinity of these reductions (such as the 8/5, the 11/7 and/or the 14/9), since drift damping due to the ECC mechanism is enhanced by the rational surfaces. This is in agreement with a previous study on magnetic activity during pellet injection into TJ-II (McCarthy *et al.* 2021). Starting from the right, the second and third points show a relatively smaller drift. However, these points correspond to the beginning of the ablation phase, and therefore it is not possible to determine whether these low drift values are due

https://doi.org/10.1017/S0022377823001010 Published online by Cambridge University Press

to the 8/5 rational surface, located at $\rho = \sim 0.756$, or to the fact that the plasmoids are small at the beginning of the ablation, and hence the drift displacement is shorter. Then, in the range of $\sim 0.6 \leq \rho \leq \sim 0.65$ (forth to sixth points from the right), the drift increases, while its value remains approximately constant in the range of $\sim 0.4 \leq \rho \leq \sim 0.6$ (sixth to eleventh points from the right). It is possible that this limitation in the drift is caused by the 19/12 and 11/7 rational surfaces, found at $\rho = \sim 0.623$ and $\rho = \sim 0.495$, respectively. Following this, the drift increases again (twelfth point), to decrease once more in the range of $\sim 0.25 \leq \rho \leq \sim 0.35$ (twelfth to fifteenth points from the right) and increase afterwards (fifteenth and sixteenth points from the right). This local minimum in the drift could be attributed to the 11/7 rational surface, although it may be located too far from the origins of these plasmoids to have any effect so early in the homogenisation process. Thereafter, plasmoids (points 16 to 21 from the right, in the range of $\sim 0.06 \leq \rho \leq \sim 0.16$) are detached in the vicinity of the 14/9 rational surface ($\rho = \sim 0.185$), which results in a reduction of the drift. Finally, as the plasmoids are detached close to and/or beyond the magnetic axis, the ablation rate is reduced, as are the plasmoid pressure and the drift (points 22 and 23 from the right). The importance of the observed enhancement of drift damping should depend on the distance between the origin of the plasmoid and the rational surface. For instance, if a plasmoid is created too close to a rational surface, the time of connection will be larger than the camera exposure time (1 μs in all cases considered here) and thus it is not possible to observe the effect of the rational surface. In contrast, if the connection time is longer than the exposure time, no effect will be observed either.

To verify that this is not an arbitrary result, it is important to perform injections in other configurations, with different iota profiles. For instance, results for the 100_52_66 configuration are presented now. Plasmoid drifts, averaged for a series of reproducible discharger (shots 53365–53367, which correspond to pellets with an average particle content of 7.3×10^{18} atoms injected at 886 m s^{-1} along Line 1) are plotted in figure 7, together with the iota profile of the 100_52_66 configuration, and the main rational surfaces. Fast-camera settings corresponding to these discharges are a frame rate between 50 kfps and 112.5 kfps and an exposure time of 1 μs. Again, it is observed that plasmoid drifts tend, in general, to increase slightly with pellet penetration depth. In addition, the plasmoid drift is significantly reduced at certain radial positions, which roughly coincide with the position of several low-order rational surfaces (the 5/3, the 18/11 and the 13/8). As for the other configurations studied here, the observed drift is relatively small between the first and the second points from the right. However, as this interval corresponds to the beginning of the ablation phase, it is not possible, as for the other cases described here, to determine whether this reduction is due to the 5/3 rational surface ($\rho = \sim 0.744$) or to smaller plasmoids with limited drifts. Then, in the range of $\sim 0.5 \leq \rho \leq \sim 0.7$ (from the sixth to the third points from the right), the drift increases, with a local minimum around $\rho = \sim 0.52$ (fifth point), which in principle cannot be directly attributed to any rational surface. Next, in the range of $\sim 0.2 \leq \rho \leq \sim 0.5$ (from seventh to thirteen plasmoids from the right), the drift decreases again, with two local minima at $\rho = \sim 0.3$ (eleventh point) and $\rho = \sim 0.42$ (eighth point). The former can be due to the 18/11 rational surface ($\rho = \sim 0.398$), while the latter is not directly correlated to any rational surface. Moreover, in the range of $\sim 0.0 \leq \rho \leq \sim 0.14$ (the fourteenth and sixteenth plasmoids from the right), the drift showed a further reduction, as plasmoids cross the 13/8 rational surface ($\rho = \sim 0.136$). Finally, although the number of cases included in this series and the number of data points are reduced, in general, a relationship is found between the radial region in which the plasmoid drift is reduced and the location of the rational surfaces, within the measurement uncertainty.

https://doi.org/10.1017/S0022377823001010 Published online by Cambridge University Press

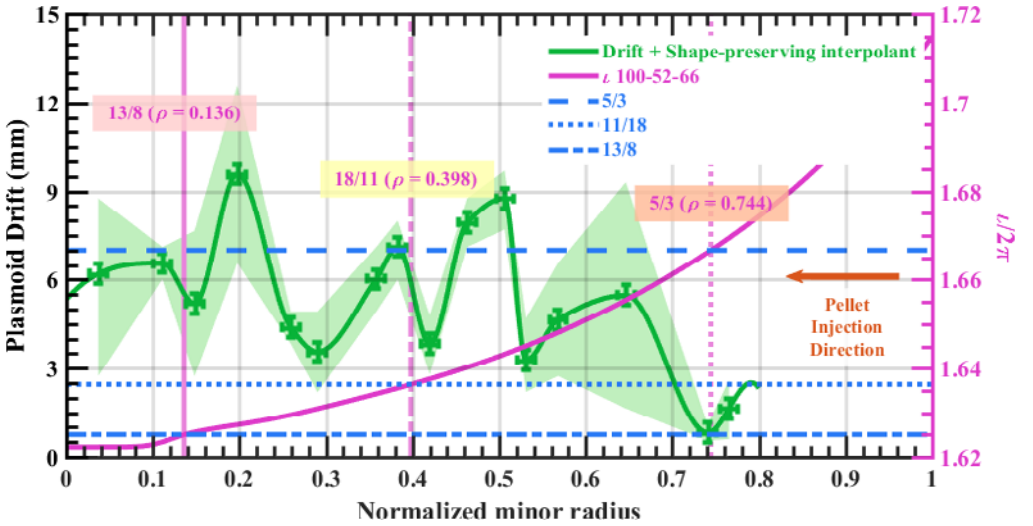

FIGURE 7. Plasmoid drift estimated from fast-camera images for TJ-II 100_52_66 configuration, and the series 53365–53367. Calculated drift values are plotted in green, with the corresponding error bars, while a connection between points is made with a solid green line. The iota profile for this configuration is plotted in solid magenta. The strongest low-order rational values in this iota interval are highlighted using horizontal dashed, dotted and dash-dotted blue lines, and vertical solid, dash-dotted and dotted magenta lines. The pellet injection direction is indicated by an orange arrow.

4. HPI2 simulations

To complete this study, the stellarator version of the previously mentioned HPI2 code (Panadero *et al.* 2018) is used to simulate pellet injection for different TJ-II configurations. Such a study allows comparing theoretical plasmoid drifts with experimental results, i.e. assuming that the origin of the plasmoid is the position of the pellet in each frame, drift values are determined from images recorded with $\sim$1 μs frame exposure time, while simulated values are calculated at the end of the homogenisation process, which is $\sim$500 μs (plasmoid origin in the simulations is also pellet position). Although there is a large difference between the two time scales and the experimental measurement cannot give an indication of the total drift displacement (once the ionisation degree of the plasmoid is high enough, it is not possible to observe it with the fast camera), both simulations and experimental data indicate that the maximum drift acceleration is reached very early in the homogenisation phase (Panadero 2018). Therefore, if the drift displacement is already smaller after 1 μs, because the drift acceleration is already damped, the total drift must necessarily be smaller, as the acceleration becomes negative almost immediately afterwards. This also implies that the general tendencies and the total displacement values should not be considered in the analysis. In addition, it must be considered that only the radial component of the drift is estimated from fast-camera images, while both the radial and the poloidal components are calculated by HPI2. However, only small radial scales are of interest for this comparison. In contrast to the experimental situation, the simulation of pellet injections into ECRH plasmas is more convenient than NBI cases as it is not necessary to include the effect of suprathermal ions, which are only important in NBI plasmas and imply additional uncertainties associated with fast ion energy and particle distribution. However, NBI scenarios are presented here as they are more convenient for the comparison with

https://doi.org/10.1017/S0022377823001010 Published online by Cambridge University Press

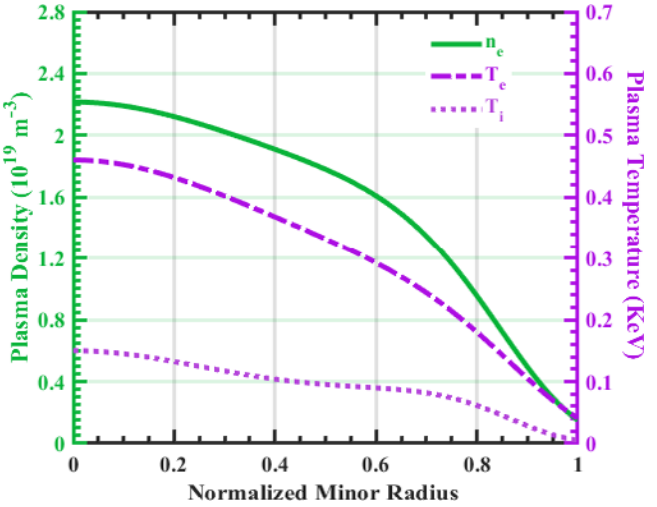

FIGURE 8. Electron density (solid green line), as well as electron and ion temperatures (dash-dotted and dotted purple lines, respectively), profiles corresponding to a representative balanced NBI discharge in TJ-II. Electron density and temperature profile are obtained from the fitting of the Thomson scattering measurements of a typical NBI plasma in TJ-II, while the ion temperature profile is assumed to be proportional to the electron temperature profile, with a central value of 120 eV.

experiments. In addition, representative plasma scenarios and average pellet parameters are chosen, i.e. simulation results shown here do not correspond to a particular case. Instead, the plasma profiles used as input to HPI2 are generalised Gaussians fitted from Thomson scattering measurements of representative balanced NBI discharges, while the chosen input pellet size and speed values are averaged values for the experimental session considered in this study. This is done as the aim of this study is a comparison of the magnetic configurations of interest with similar plasma conditions. It should be noted that, for simplicity, a mono-energetic beam of fast ions is considered in the simulation and the pitch angle is neglected. Considering the parameters of the NBIs ($P_{\mathrm{NBI1}} = 430$ kW, $V_{\mathrm{NBI1}} = 30$ kV and $I_{\mathrm{NBI1}} = 40$ A; $P_{\mathrm{NBI2}} = 390$ kW, $V_{\mathrm{NBI2}} = 27$ kV and $I_{\mathrm{NBI2}} = 38$ A), an energy of 30 keV is used for the beam. In addition, to construct the density distribution, apart from the NBI parameters, the results from Bustos *et al.* (2011) are used, i.e. a fast ion distribution with a maximum around $\rho \sim 0.4$ (see figure 2 of Bustos *et al.* 2011). Moreover, an addition peak in the distribution around $\rho \sim 0.65$ is considered to account for the observed over-ablation in the H_α signals around this point. In all cases, the injection geometry corresponds to Line 1 (see figure 2*a*). Furthermore, vacuum magnetic configurations are considered in the simulation; however, changes in the iota profile are not expected for the experimental conditions considered here (Lopez-Bruna *et al.* 2006; McCarthy *et al.* 2015*b*). The spatial resolution for the ablation calculation is set at 2 mm, this being sufficient for a plasma with a minor radius of the order of 20 cm. No *ad hoc* assumptions are made for the spatial resolution or for the number of plasmoids or striations. The density and temperature profiles used in the simulation are shown in figure 8. First, for the standard configuration, the pellet parameters considered are 9×10^{18} H atoms and 900 m s^{-1}. The resultant ablation profile is compared with the H_α emission of discharge 53346, a representative pellet injection case into balanced NBI plasmas (see figure 9). It is noted that the agreement is significantly good.

https://doi.org/10.1017/S0022377823001010 Published online by Cambridge University Press

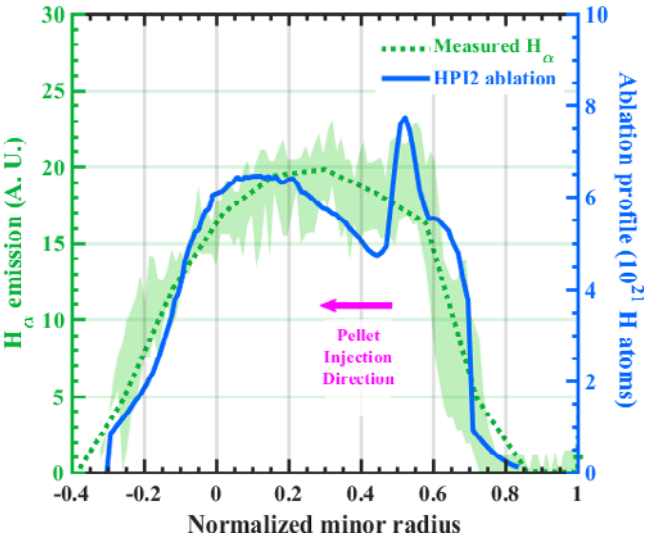

FIGURE 9. HPI2 simulated ablation (solid blue line) profile compared with measured H_α emission profiles (dotted green line, arbitrary units) for a pellet injected along Line 1 (0.9×10^{19} H atoms, velocity = 900 m s^{-1}) into the TJ-II standard configuration, 100_44_64, during the balanced NBI phase of a series of reproducible discharge (53344–53349) with density and temperature profiles shown in figure 8. The pellet injection direction is indicated by a magenta arrow.

Plasmoid drifts predicted by HPI2, as a function of the radial position where each plasmoid originates, are shown in figure 10 for the 100_44_64 configuration. In addition, the drift calculated by HPI2 when the ECC effect is neglected is also shown here. For the latter case, it is seen that the drift increases continuously with pellet penetration, without any local minima, and that all plasmoids drift from their detachment position to the last closed flux surface (LCFS), where they exit the plasma, i.e. the simulated total drift as a function of pellet position without ECC presents a linear behaviour everywhere. In contrast, when the ECC effect is considered in the simulation, in addition to the trend of increasing drift with pellet penetration, i.e. with increasing electron temperature, different regions where the drift is reduced are observed. For instance, a first region (first shaded region from the right), corresponding to plasmoids detached from the pellet in the range of $\sim 0.7 \leq \rho \leq \sim 0.76$, is identified. This reduction in the drift can be explained by the enhancement of the ECC effect caused by the 8/5 rational surface ($\rho = \sim 0.756$) on plasmoids originating in its vicinity, which suffer a small but measurable drift deceleration that prevents them from reaching the LCFS. In addition, a second region, corresponding to plasmoids born in the range of $\sim 0.22 \leq \rho \leq \sim 0.5$ (second shaded region from the right) is observed. Inside this interval, plasmoids exhibit a clear drift reduction as they pass through other low-order rational surfaces, such as the 11/7 ($\rho = \sim 0.495$) and the 19/12 ($\rho = \sim 0.623$) (see figure 3) on their way to the LCFS. Finally, a third region can be distinguished (third shaded region from the right) for plasmoids originated in the range of $0 \leq \rho \leq \sim 0.18$. For these plasmoids, the reduction of the drift can be caused by the 14/9 rational surface ($\rho = \sim 0.186$) and/or the magnetic axis. Moreover, predicted plasmoid drifts are compared with experimental values in this figure. It can be observed here that drift reductions, between error bars, in the experimental observations occur in general around the same radial positions as were identified from simulations. As already

https://doi.org/10.1017/S0022377823001010 Published online by Cambridge University Press

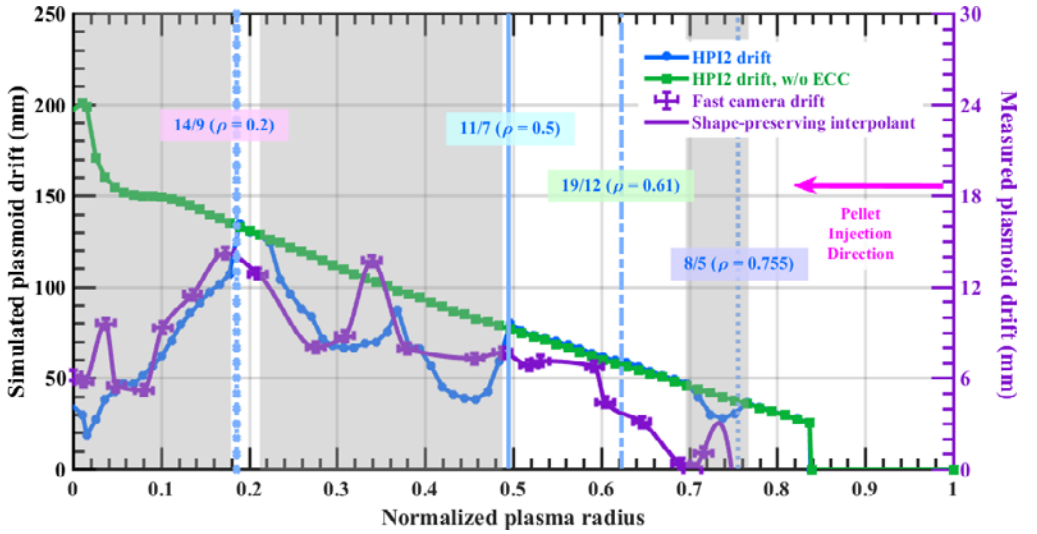

FIGURE 10. HPI2 simulated plasmoid drift at the end of the homogenisation phase (solid blue line with circles) for a pellet injected along Line 1 (0.9×10^{19} H atoms, velocity = 900 m s^{-1}) into the TJ-II standard configuration (100_44_64), during the NBI phase of a representative discharge with density and temperature profiles shown in figure 8. This is compared with the calculated drift when the ECC effect is neglected in the HPI2 simulation (solid green line with circles). In addition, these are compared with the measured drift from fast-camera images, at $t \leq 1$ μs (purple, with error bars). The pellet injection direction is indicated by a magenta arrow. It should be noted that for the simulation results, there is one plasmoid for each of the points at which ablation is calculated, while for the fast-camera data, the number of plasmoids is limited by the frame rate.

mentioned, the simulated magnitude of the drift does not match the experimental one, due to the large difference in time scales. In addition, the reduction in the drift for plasmoids born in the range of $\sim 0.4 \leq \rho \leq \sim 0.5$ is not clearly observed in the fast-camera data because the exposure time (1 μs) is probably too short for the plasmoid to reach the 19/12 rational surface.

To facilitate the interpretation of these results, plasmoid trajectories simulated by HPI2 are shown in figure 11. Here, it is observed that, similarly to observations reported by McCarthy *et al.* (2021), drifting plasmoids show negligible interaction with rational surfaces when they have detached from the pellet at $\rho \geq \sim 0.45$. However, plasmoids originated in the range of $\sim 0.7 \leq \rho \leq \sim 0.75$ are an exception, as their drift is reduced by the effect of the 8/5 rational surface. In contrast, plasmoids that detach deeper inside the plasma are significantly decelerated by interactions with one or more rational surfaces (14/9, 11/7 and/or 19/12). Next, the variation of plasmoid drift velocity due to the interaction with rational surfaces for several plasmoid detachment positions is shown in figure 12(*a*) (for clarity, trajectories corresponding to these plasmoids are plotted in figure 12*b*). In this figure, when the plasmoid drift velocity is observed to suddenly stop at a non-zero value, it implies that the plasmoid has left the LCFS. In contrast, when the drift velocity tends smoothly to zero, it means that the plasmoid can be fully homogenised in the plasma. Indeed, as observed here, the drift velocity of plasmoids originated around $\rho = \sim 0.5$ (plasmoid 38) and $\rho = \sim 0.48$ (plasmoid 39) evolves without any clear interaction with rational surfaces until they exit the LCFS, 18 μs and 28 μs, respectively, after cloud creation. However, for plasmoids originating at slightly deeper

https://doi.org/10.1017/S0022377823001010 Published online by Cambridge University Press

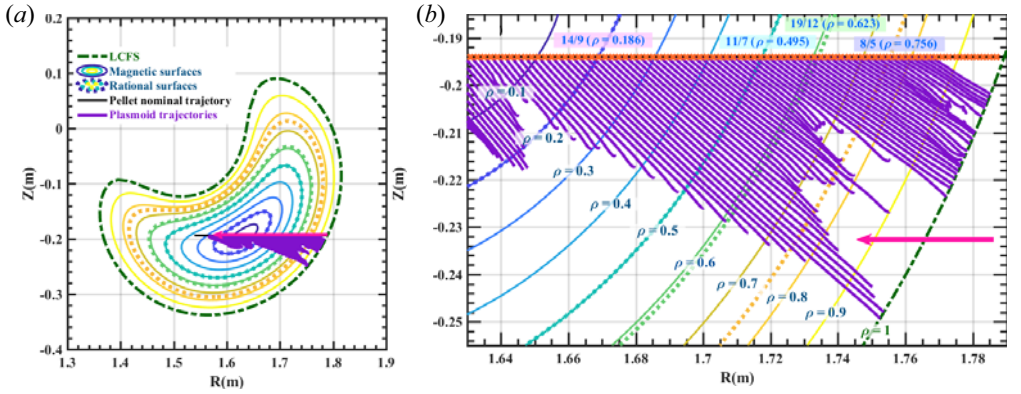

FIGURE 11. (*a*) Individual plasmoid trajectories simulated by HPI2 (solid purple lines) for a pellet injection into a TJ-II NBI plasma. Poloidal cross-sections of closed flux surfaces (solid lines) and rational surfaces (dotted lines) corresponding to the standard (100_44_64) configuration are also shown. The pellet injection direction is indicated by a magenta arrow. (*b*) Close-up of the outer plasma region. Orange crosses along the horizontal pellet trajectory correspond to individual positions for which pellet ablation and plasmoid evolution are calculated. The relationship between the normalised minor radius and R for $Z = -0.194$ (pellet injection Line 1) can be found in figure 2(*b*).

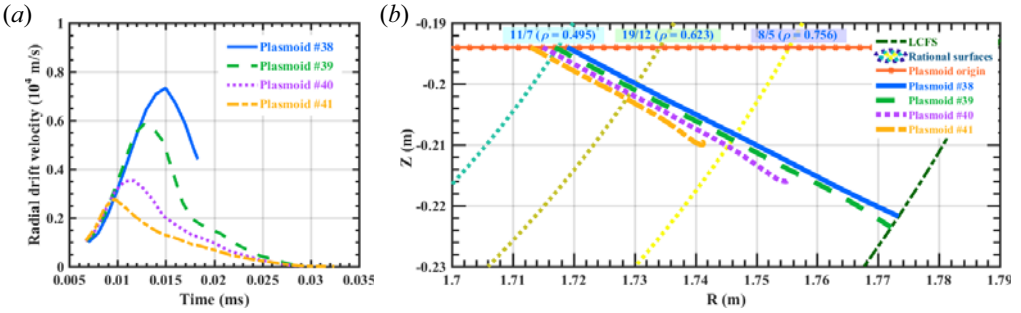

FIGURE 12. Simulated (*a*) evolution of the plasmoid drift velocity and (*b*) plasmoid trajectories, during the homogenisation phase, for plasmoid 34 (solid blue line), originating at $\rho \sim 0.52$; plasmoid 36 (dashed green line), originating at $\rho \sim 0.50$; plasmoid 40 (dotted purple line), originating at $\rho \sim 0.45$; and plasmoid 41 (dash-dotted orange line), originating at $\rho \sim 0.43$. They correspond to a pellet injected along Line 1 into a balanced NBI plasma of the TJ-II standard configuration (profiles are found in Figure 8).

depths ($\rho = \sim 0.46$ and $\rho = \sim 0.47$ – plasmoids 40 and 41, respectively), the enhancement of the ECC by the rational surfaces is clearly appreciated, as the initial drift acceleration is prematurely stopped and plasmoids evolve without reaching the LCFS until they are fully homogenised, 30 μs after cloud creation.

This same analysis is repeated now for the 100_52_66 configuration, also using the plasma temperature and density profiles shown in figure 8, pellet particle content of 9×10^{18} H atoms and pellet speed of 900 m s^{-1} as input for the simulation. Plasmoid drifts predicted by HPI2, as a function of the radial position where these plasmoids originate for this configuration, are shown in figure 13, with and without the inclusion of the ECC effect. First, a linear behaviour is predicted when the ECC is neglected in the

https://doi.org/10.1017/S0022377823001010 Published online by Cambridge University Press

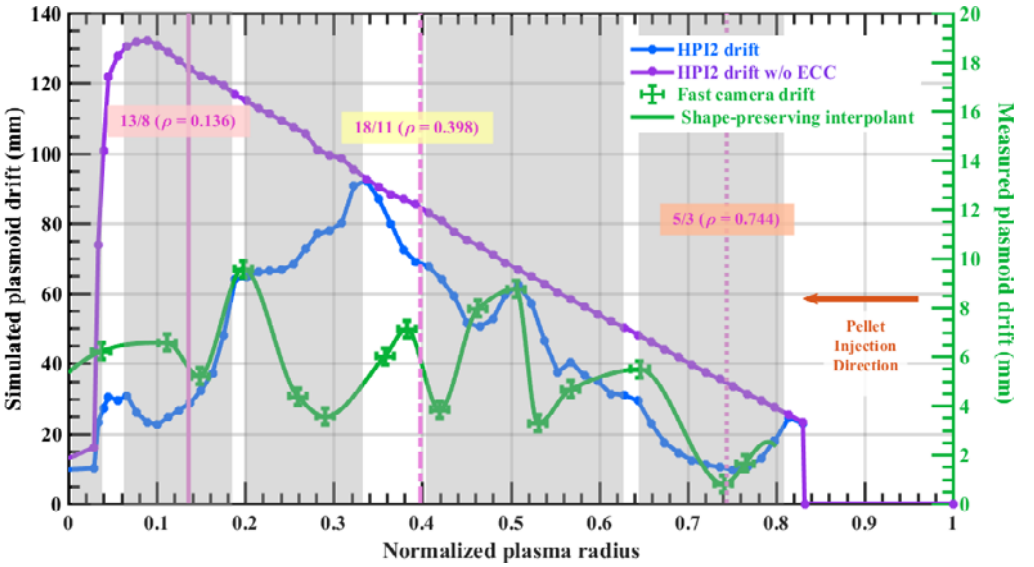

FIGURE 13. HPI2 simulated plasmoid drift at the end of the homogenisation phase (solid blue line with circles) for a pellet injected along Line 1 (9×10^{18} H atoms, velocity = 900 m s^{-1}) into the TJ-II configuration 100_52_66, during the balanced NBI phase of a typical discharges with density and temperature profiles shown in figure 8. This is compared with the calculated drift when the ECC effect is neglected in the HPI2 simulation (solid purple line with squares). In addition, these are compared with the measured drift from fast-camera images, at $t \leq 1$ μs (green, with error bars). The pellet injection direction is indicated by an orange arrow. It should be noted that for the simulation results, there is one plasmoid for each of the points at which ablation is calculated, while for the fast-camera data, the number of plasmoids is limited by the frame rate.

simulation, i.e. the drift increases continuously with pellet penetration, from the origins of the plasmoids to the LCFS, where the majority of the plasmoids are lost. In contrast, when the ECC effect is included in the simulation, plasmoid drifts are reduced almost everywhere. For instance, in the first shaded area from the right in figure 13, a reduction of the drift caused by the 5/3 rational surface is observed. Then, within the second shaded area from the right, the drift increases, but it is still smaller than the drift without the ECC effect. This is attributed the 5/3 rational surface, which is crossed by these plasmoids later in the homogenisation phase. Next, within the third shaded region, the effect of the 18/11 rational surface on the drift decrease is noted. Afterwards, a reduction caused by the 13/8 rational surface is observed within the fourth shaded region. Finally, an additional reduction (fifth shaded region) can be attributed to the fact that plasmoids are crossing the magnetic axis. Moreover, these results are compared with the experimental ones (see figure 7). It is observed again that both measured and calculated drift reductions occur around the same radial positions as a consequence of the enhanced damping close to the rational surfaces. This implies that the drift reduction observed in the experiment around $\rho = \sim 0.55$, which could not be directly linked to a rational surface, is indeed caused by one. However, the reduction of the drift measured around $\rho = \sim 0.42$ cannot be explained by a rational surface. The limited number of available cases may explain this disagreement, in addition to the frame rate, which may not have been sufficiently high.

Moreover, the plasmoid trajectories simulated by HPI2 are shown in figure 14 to facilitate also for the 100_52_66 case the interpretation of these results. Here, it is observed

https://doi.org/10.1017/S0022377823001010 Published online by Cambridge University Press

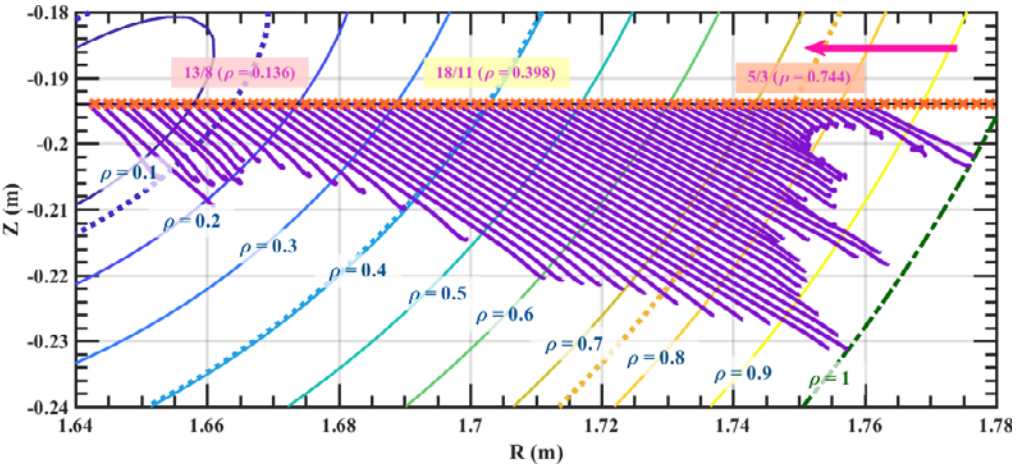

FIGURE 14. Close-up of the outer plasma region showing individual plasmoid trajectories simulated by HPI2 (solid purple lines) for a pellet injection into a TJ-II NBI plasma. Poloidal cross-section of closed flux surfaces (solid lines) and rational surfaces (dotted lines) corresponding to the 100_52_66 configuration is also shown . The pellet injection direction is indicated by a magenta arrow. Orange crosses along the horizontal pellet trajectory correspond to individual positions for which pellet ablation and plasmoid evolution are calculated. The relationship between the normalised minor radius and R for $Z = -0.194$ (pellet injection Line 1) can be found in figure 2(*b*).

that plasmoids that detached in the vicinity of a rational surface present a significantly reduced drift that prevents them from reaching the LCFS. For these plasmoids, the enhancement of the ECC by rational surfaces is clearly shown in figure 15(*a*), where the variation of plasmoid drift velocity due to the interaction with rational surfaces, depending on where the plasmoid is detached, is shown (for illustration purposes, trajectories corresponding to these plasmoids are also plotted in figure 15*b*). For this configuration, the drift velocity of a plasmoid originated around $\rho = \sim 0.34$ (plasmoid 104 in this figure) evolves without any clear effect of rational surfaces until it leaves the LCFS, ~ 23 μs after cloud creation. However, as for the standard configuration, the enhancement of the ECC by the rational surfaces is clear for plasmoid originated at deeper depths ($\rho \sim 0.31$, $\rho \sim 0.28$ and $\rho \sim 0.19$ for plasmoids 106, 109 and 115, respectively), as the initial drift acceleration is prematurely stopped, especially for plasmoid 115.

Finally, the simulation results of these two configurations, the standard and the 100_52_66, are compared to determine whether rational surface locations play a clear role in pellet ablation and particle deposition. As observed in figure 16, similar ablation profiles are obtained for both cases, particularly for $\rho \geq 0.4$. However, having similar ablation profiles, deposition profiles are seen to differ significantly. Indeed, although the maxima of the pellet particle deposition profile are similar ($\rho \sim 0.15$), the maximum deposition is significantly higher for the 100_52_66, which is more beneficial from the point of view of an efficient fuelling. To clearly appreciate the differences in plasmoid drift for these two configurations, total drifts calculated for each plasmoid are plotted in figure 17. It is observed here that, except for $\rho \geq 0.8$, for which drifts are basically identical, there are large differences for plasmoid drifts between configurations due to the presence of different low-order rational surfaces and their radial location. (It should be noted that the averaged minor radius of the 100_52_66 configuration ($a_0 = 0.2$ m) is slightly larger than the one of the standard configuration ($a_0 = 0.19$ m)).

https://doi.org/10.1017/S0022377823001010 Published online by Cambridge University Press

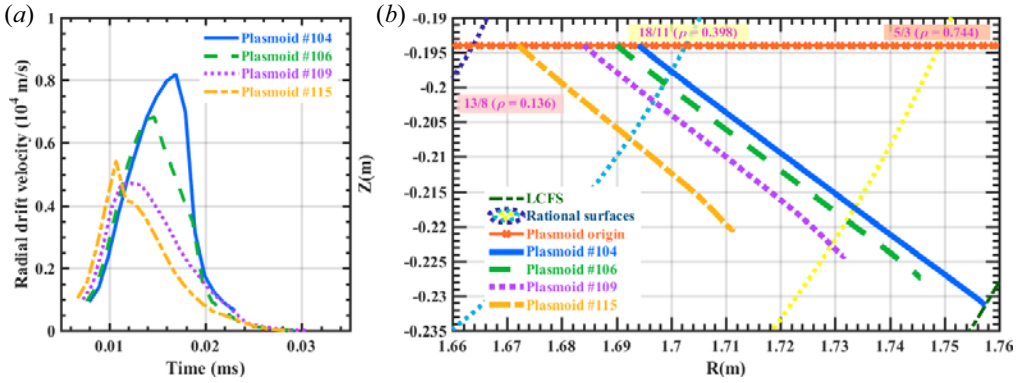

FIGURE 15. Simulated evolution of the plasmoid drift velocity, during the homogenisation phase, for plasmoid 104 (solid blue line), originating at $\rho \sim 0.34$; plasmoid 106 (dashed green line), originating at $\rho \sim 0.31$; plasmoid 109 (dotted purple line), originating at $\rho \sim 0.28$; and plasmoid 115 (dash-dotted orange line), originating at $\rho \sim 0.19$. These correspond to a pellet injection along Line 1 into a NBI plasma of the TJ-II 100_52_66 configuration.

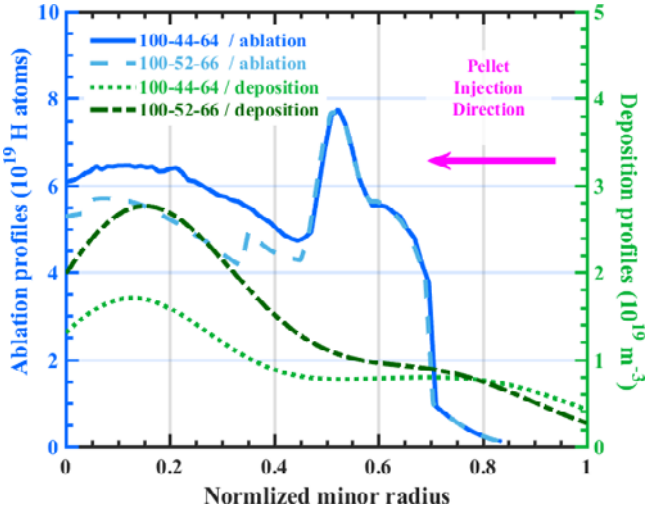

FIGURE 16. HPI2 simulated ablation (solid and dashed blue lines) and deposition (dash-dotted and dotted green lines) profiles for the TJ-II standard configuration (solid blue and dotted green lines) and configuration 100_52_66 (dashed blue and dash-dotted green lines). They correspond to a pellet injected along Line 1 into the balanced NBI phase. The pellet injection direction is indicated by a magenta arrow.

5. Conclusions and summary

In this work, hydrogen pellets have been injected into NBI-heated TJ-II plasmas made using different magnetic configurations to study the influence of rational surfaces on plasmoid drift in stellarators. For this purpose, fast-camera images have been used to estimate the drift. In this section, the main results of this study are summarised and the principal conclusions are presented. The first result to highlight is that the plasmoid drift is systematically reduced at certain radial positions. These positions are in the vicinity of some of the main low-order rational surfaces of the TJ-II standard magnetic

https://doi.org/10.1017/S0022377823001010 Published online by Cambridge University Press

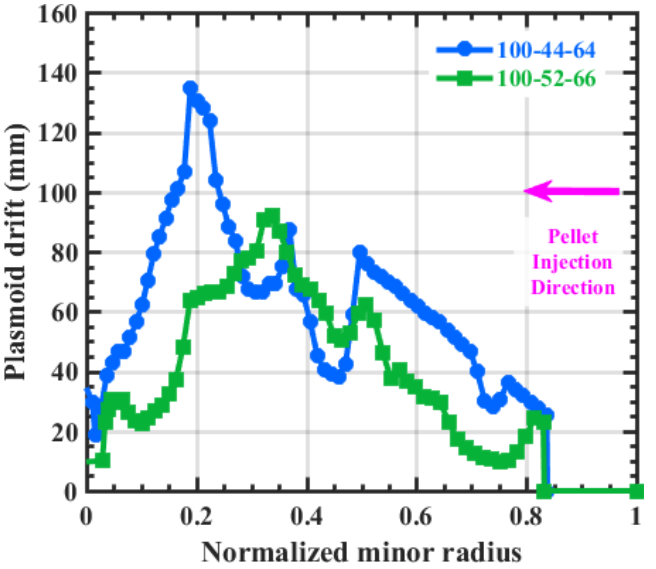

FIGURE 17. HPI2 plasmoid drift for the TJ-II standard configuration (blue line with circles) and configuration 100_52_66 (green line with squares). They correspond to a pellet injected along Line 1 into the balanced NBI phase. The pellet injection direction is indicated by a magenta arrow.

configuration. Next, it has been observed that, when changing magnetic configuration, the positions where the plasmoid drift is reduced are shifted with respect to the 100_44_64 positions, in accordance with the position of the main low-order rational surfaces of the new configuration. Furthermore, when these experimental results are compared with HPI2 simulations for representative plasma scenarios, it is observed that predicted drift reductions occur approximately at the same positions as measured ones. Therefore, these results imply that such reductions can be attributed to the ECC effect, as it is most effective at damping the drift acceleration close to rational surfaces. Finally, when ablation and deposition profiles calculated with HPI2 for two different TJ-II magnetic configurations are compared, it is found that, even though similar ablation profiles are predicted, significantly different deposition profiles are obtained, this being attributed to significant variations in plasmoid drift. However, an experimental confirmation of such differences in the deposition profiles remains to be obtained, as the dispersion in the density profiles measured with a Thomson scattering system are larger than the expected differences between configurations. An attempt will be made to address this experimental comparison in future work.

Having summarised the most relevant results, the main conclusions are now recapitulated. From the results presented here, it can be first concluded that the ECC, normally neglected in stellarators as it is considered a second order with respect to the ICC effect, can play an important role in modifying the plasmoid drift. In addition, it is concluded that magnetic configuration can be used to improve pellet fuelling and particle deposition. Thus, it may be possible to achieve relatively deep and efficient fuelling using LFS pellets in stellarators. This may be a critical point, since, to the best of the authors' knowledge, no significant differences between LFS and HFS pellets in stellarators have been reported to date.

https://doi.org/10.1017/S0022377823001010 Published online by Cambridge University Press

Acknowledgements

Views and opinions expressed are those of the author(s) only and do not necessarily reflect those of the European Union or the European Commission. Neither the European Union nor the European Commission can be held responsible for them.

Editor Per Helander thanks the referees for their advice in evaluating this article.

Declaration of interests

The authors report no conflict of interest.

Funding

This work has been carried out within the framework of the EUROfusion Consortium, funded by the European Union via the Euratom Research and Training Programme (Grant Agreement No 101052200 - EUROfusion). This work was supported by the Spanish *Ministerio de Ciencia e Innovacion*, MCIN/AEI/10.13039/501100011033, (N.P., K.J.M., I.G.C., J.H.S., grant number PID2020-116599RB-I00).

REFERENCES

BUSTOS, A., CASTEJÓN, F., OSAKABE, M., FERNÁNDEZ, L.A., MARTIN-MAYOR, V., GUASP, J. & FONTDECABA, J.M. 2011 Kinetic simulations of fast ions in stellarators. *Nucl. Fusion* **51** (8), 083040.

COMBS, S.K., FOUST, C.R., MCGILL, J.M., CAUGHMAN, J.B.O., MCCARTHY, K.J., BAYLOR, L.R., CHAMORRO, M., FEHLING, D.T., GARCIA, R., HARRIS, J.H., *et al.* 2013 Results from laboratory testing of a new four-barrel pellet injector for the TJ-II stellarator. *Fusion Sci. Technol*. **64** (3), 513–520.

COMMAUX, N., PÉGOURIÉ, B., BAYLOR, L.R., KÖCHL, F., PARKS, P.B., JERNIGAN, T.C., GÉRAUD, A. & NEHME, H. 2010 Influence of the low order rational q surfaces on the pellet deposition profile. *Nucl. Fusion* **50** (2), 025011.

GEULIN, E. & PEGOURIE, B. 2022 Pellet core fueling in tokamaks, stellarators and reversed field pinches. *Plasma Fusion Res*. **17**, 2102101.

HIDALGO, C., ASCASÍBAR, E., ALEGRE, D., ALONSO, A., ALONSO, J., ANTÓN, R., BACIERO, A., BALDZUHN, J., BARCALA, J.M., BARRERA, L., *et al.* 2022 Overview of the TJ-II stellarator research programme towards model validation in fusion plasmas. *Nucl. Fusion* **62** (4), 042025.

KÖCHL, F., PEGOURIE, B., MATSUYAMA, A., NEHME, H., WALLER, V., FRIGIONE, D., GARZOTTI, L., KAMELANDER, G. & PARAIL, V. 2012 *Modelling of pellet particle ablation and deposition: the hydrogen pellet injection code HPI2*. Preprint EFDA–JET–PR(12)57, 82.

LENGYEL, L. 1978 Pellet ablation in hot plasmas and the problem of magnetic shielding. *Phys. Fluids* **21** (11), 1945.

LOPEZ-BRUNA, D., CASTEJÓN, F., ROMERO, J.A., ESTRADA, T., MEDINA, F., OCHANDO, M., LOPEZ-FRAGUAS, A., ASCASIBAR, E., HERRANZ, J., SANCHEZ, E., *et al.* 2006 Magnetic shear and transport in ECRH discharges of the TJ-ii under ohmic induction, Madrid (Spain). Available at http://inis.iaea.org/Search/search.aspx?orig_q=RN:38030360

MAAßBERG, H., BEIDLER, C.D. & SIMMET, E.E. 1999 Density control problems in large stellarators with neoclassical transport. *Plasma Phys. Control. Fusion* **41** (9), 1135–1153.

MATSUYAMA, A., KÖCHL, F., PÉGOURIÉ, B., SAKAMOTO, R., MOTOJIMA, G. & YAMADA, H. 2012*a* Modelling of the pellet deposition profile and ∇ B -induced drift displacement in non-axisymmetric configurations. *Nucl. Fusion* **52** (12), 123017.

MATSUYAMA, A., PÉGOURIÉ, B., SAKAMOTO, R., MISHRA, J.S., MOTOJIMA, G. & YAMADA, H. 2012*b* Over-ablation and deflection of hydrogen pellets injected into neutral beam injection heated plasmas in the large helical device. *Plasma Phys. Control. Fusion* **54** (3), 35007.

MCCARTHY, K.J., PANADERO, N., ARAPOGLOU, I., COMBS, S.K., CAUGHMAN, J.B.O., DE LA CAL, E., FOUST, C., GARCÍA, R., HERNÁNDEZ SÁNCHEZ, J., MARTÍN, F., *et al.* 2015*a* The pellet

https://doi.org/10.1017/S0022377823001010 Published online by Cambridge University Press

injector and its associated diagnostics for performing plasma studies on the TJ-II stellarator. In *1st EPS Conference on Plasma Diagnostics, Proceedings of Science (ECPD)*, vol. 134, Frascati (Italy). Proceedings of Science (https://pos.sissa.it/).

McCarthy, K.J., Panadero, N., Velasco, J.L., Combs, S.K., Caughman, J.B.O., Fontdecaba, J.M., Foust, C.R., García, R., Hernández Sánchez, J., Navarro, M., *et al.* 2017 Plasma fuelling with cryogenic pellets in the stellarator TJ-II. *Nucl. Fusion* **57** (5), 056039.

McCarthy, K.J., Ascasíbar, E., Tamura, N., Panadero, N., García-Cortes, I., Van Milligen, B., Cappa, A., García, R., Hernández-Sánchez, J., Liniers, M., *et al.* 2021 The interpretation of magnetic activity associated with pellet injections into plasmas created in the stellarator TJ-II. *Nucl. Fusion* **61** (7), 076014.

McCarthy, K.J., Panadero, N., López-Fraguas, A., Hernández, J. & van Milligen, B.P. 2015*b* A spectrally resolved motional stark effect diagnostic for the TJ-II stellarator. *Contrib. Plasma Phys.* **55** (6), 459–469.

Mikkelsen, M.R., McGuire, K.M., Schmidt, G.L., Zweben, S.J., Attenberger, S.E., Houlberg, W.A. & Milora, S.L. 1995 Core fuelling to produce peaked density profiles in large tokamaks. *Nucl. Fusion* **35** (5), 521–533.

Milora, S.L., Mertens, V., Houlberg, W.A. & Lengyel, L. 1995 Review paper: pellet fuelling. *Nucl. Fusion* **35** (6), 657–754.

Müller, H.W., Büchl, K., Kaufmann, M., Lang, P.T., Lang, R.S., Lorenz, A., Maraschek, M., Mertens, V. & Neuhauser, J. 1999 High-β plasmoid drift during pellet injection into tokamaks. *Phys. Rev. Lett.* **83** (11), 2199–2202.

Panadero, N. 2018 A study of the physics of pellet injection in magnetically confined plasmas in stellarators. PhD thesis, Universidad Carlos III de Madrid.

Panadero, N., McCarthy, K.J., Koechl, F., Baldzuhn, J., Velasco, J.L., Combs, S.K., de la Cal, E., García, R., Hernández-Sánchez, J., Silvagni, D., *et al.* 2018 Experimental studies and simulations of hydrogen pellet ablation in the stellarator TJ-II. *Nucl. Fusion* **58** (2), 026025.

Panadero, N., Koechl, F., Polevoi, A.R., Baldzuhn, J., Beidler, C.D., Lang, P.T., Loarte, A., Matsuyama, A., McCarthy, K.J., Pégourié, B., *et al.* 2023 A comparison of the influence of plasmoid-drift mechanisms on plasma fuelling by cryogenic pellets in ITER and Wendelstein 7-X. *Nucl. Fusion* **63** (4), 046022.

Panadero, N., Medina, D., McCarthy, K.J., Kocsis, G., Szepesi, T., Motojima, G., de la Cal, E., Hernandez-Sanchez, J. & Ros, A. 2021 Pellet studies with an upgrade fast camera system in the stellarator TJ-II. In *ECA Vol. 45A (47th European Physical Society Conference on Plasma Physics, EPS 2021)*, Sitges (Barcelona, Spain). Available at http://ocs.ciemat.es/EPS2021PAP/pdf/P3.1005.pdf

Parks, P.B. & Baylor, L.R. 2005 Effect of parallel flows and toroidicity on cross-field transport of pellet ablation matter in tokamak plasmas. *Phys. Rev. Lett.* **94** (12), 1–4.

Pégourié, B. 2007 Review: pellet injection experiments and modelling. *Plasma Phys. Control. Fusion* **49** (8), R87–R160.

Pégourié, B., Waller, V., Dumont, R.J., Eriksson, L.-G., Garzotti, L., Géraud, A. & Imbeaux, F. 2005 Modelling of pellet ablation in additionally heated plasmas. *Plasma Phys. Control. Fusion* **47** (1), 17–35.

Pégourié, B., Waller, V., Nehme, H., Garzotti, L. & Geraud, A. 2007 Homogenization of the pellet ablated material in tokamaks taking into account the ∇B-induced drift. *Nucl. Fusion* **47** (1), 44–56.

Rozhansky, V.A., Senichenkov, I.Y., Veselova, I.Y. & Schneider, R. 2004 Mass deposition after pellet injection into a tokamak. *Plasma Phys. Control. Fusion* **46** (4), 575–591.

Sakamoto, R., Pégourié, B., Clairet, F., Géraud, A., Gil, C., Hacquin, S. & Köchl, F. 2013 Cross-field dynamics of the homogenization of the pellet deposited material in Tore Supra. *Nucl. Fusion* **53** (6), 063007.

Senichenkov, I.Y., Veselova, I.Y., Rozhansky, V.A. & Schneider, R. 2005 Modeling of the pellet cloud structure in the presence of ∇B induced drift. *J. Nucl. Mater.* **337–339**, 446–450.

https://doi.org/10.1017/S0022377823001010 Published online by Cambridge University Press

TABARÉS, F.L., OCHANDO, M.A., MEDINA, F., TAFALLA, D., FERREIRA, J.A., ASCASIBAR, E., BALBÍN, R., ESTRADA, T., FUENTES, C., GARCÍA-CORTÉS, I., *et al.* 2008 Plasma performance and confinement in the TJ-II stellarator with lithium-coated walls. *Plasma Phys. Control. Fusion* **50** (12), 124051.

TABARÉS, F.L., OCHANDO, M., TAFALLA, D., MEDINA, F., MCCARTHY, K., FONTDECABA, J.M., LINIERS, M., GUASP, J., ASCASÍBAR, E., ESTRADA, T., *et al.* 2010 Energy and particle balance studies under full boron and lithium-coated walls in TJ-II. *Contrib. Plasma Phys*. **50** (6–7), 610–615.

THIENPONDT, H., GARCÍA-REGAÑA, J.M., CALVO, I., ALONSO, J.A., VELASCO, J.L., GONZÁLEZ-JEREZ, A., BARNES, M., BRUNNER, K., FORD, O., FUCHERT, G., *et al.* 2023 Prevention of core particle depletion in stellarators by turbulence. *Phys. Rev. Res*. **5** (2), L022053.

https://doi.org/10.1017/S0022377823001010 Published online by Cambridge University Press